

## Evolution of Mixed Rossby–Gravity Waves in Idealized MJO Environments

ANANTHA R. AIYYER AND JOHN MOLINARI

*Department of Earth and Atmospheric Sciences, The University at Albany, State University of New York, Albany, New York*

(Manuscript received 9 December 2002, in final form 21 May 2003)

### ABSTRACT

A linear shallow water model is used to simulate the evolution of mixed Rossby–gravity (MRG) waves in background states representative of the convective phase of the Madden–Julian oscillation (MJO). Initial MRG wave structures are obtained analytically. The MJO basic state is defined by the steady response of the tropical atmosphere to localized heating. Results from the simulations reveal that variations in the background flow play a significant role in the evolution of the MRG waves. When the basic state is symmetric about the equator, the MRG wave amplifies within the convergent region of the background flow and the ensuing development remains symmetric. When the heating is asymmetric, both the basic state and the MRG wave evolution exhibit significant asymmetries. Prominent features of this simulation are the development and growth of a series of small-scale, off-equatorial eddies that resemble tropical-depression-type disturbances.

The results suggest that a persistent large-scale heating that is asymmetric with respect to the equator may lead to the growth of off-equatorial disturbances from an equatorial mode. These disturbances, approximately 1000–2000 km in scale, are considerably smaller than the initial wavelength of the MRG wave. It is suggested that the cyclonic elements among them could serve as seedlings for tropical cyclones. This process may be particularly relevant to cyclogenesis in the tropical western Pacific, a region where the MJO and MRG waves are frequently observed.

### 1. Introduction

Observations in the Tropics reveal variability on a wide range of space scales and timescales. A fundamental advancement in our understanding of equatorial variability was made by Matsuno (1966) when he derived the dispersion relations and structures for wave solutions of the shallow water equations on an equatorial  $\beta$  plane. Since then, numerous theoretical and observational investigations of equatorial waves have been conducted (Yanai and Maruyama 1966; Wallace and Kousky 1968; and many others). In their study of wave-number–frequency spectra in the outgoing longwave radiation (OLR), Wheeler and Kiladis (1999) detected convectively coupled equatorial waves that matched theoretical dispersion relations. A detailed survey of past work on equatorial waves can be found in Wheeler and Kiladis (1999) and Wheeler et al. (2000).

Among the various synoptic-scale disturbances that are observed in the Tropics, mixed Rossby–gravity (MRG) waves and off-equatorial easterly waves [commonly referred to as tropical-depression-type (TD-type) disturbances] have recently become a focus of attention owing to their possible role in tropical cyclogenesis. In

the central Pacific, MRG waves have wavelengths of 6000–10 000 km and phase speeds of 15–20 m s<sup>-1</sup> (Liebmann and Hendon 1990; Dunkerton and Baldwin 1995; Takayabu and Nitta 1993). In the western Pacific, MRG wave scales are generally smaller (Liebmann and Hendon 1990), and cases with wavelengths around 3000 km and phase speeds of 3.5–4 m s<sup>-1</sup> have been reported in observations (Dickinson and Molinari 2002). TD-type disturbances with periods of 3–6 days (Takayabu and Nitta 1993) are often identifiable as off-equatorial wave trains with convection occurring within the low pressure cyclonic centers. In addition to synoptic-scale disturbances, the tropical atmosphere is also influenced by large-scale phenomena such as the Madden–Julian oscillation (MJO), which has a period that ranges from 20 to 80 days (Madden and Julian 1994).

Of particular interest to this study is the evolution of MRG waves into TD disturbances as described in several past studies (e.g., Takayabu and Nitta 1993, Liebmann and Hendon 1990). Liebmann and Hendon (1990) found that disturbances in the central Pacific had structures consistent with equatorially trapped MRG waves but those near 115°–140°E appeared to propagate northwestward, away from the equator. Takayabu and Nitta (1993) observed a similar connection between equatorial MRG waves and off-equatorial TD disturbances. They suggested that TD disturbances may develop as a result of the reduction of the wavelength of the MRG

---

*Corresponding author address:* Mr. Anantha R. Aiyer, Es 333, Dept. of Earth and Atmospheric Sciences, The University at Albany, State University of New York, 1400 Washington Ave., Albany, NY 12222.  
E-mail: aiyer@atmos.albany.edu

waves due to the variation in the background zonal wind. Recently, Dickinson and Molinari (2002) documented a case where TD-type features evolved within the convective envelope of the MJO over the western Pacific and showed that the source of the TD disturbances was a large-amplitude MRG wave packet. They observed that individual disturbances within the MRG wave packet amplified and turned toward the northwest during their transition to off-equatorial TD-type structures. Furthermore, they noted that three tropical cyclones formed during this period. Earlier studies by Lau and Lau (1990) and Chang et al. (1996) have established that northwestward-propagating synoptic-scale disturbances are quite common in the western Pacific.

The results of Dickinson and Molinari (2002) suggest that, in many cases, off-equatorial TD disturbances might have their origin in equatorial MRG waves and that the MJO environment may play a key role in this transformation. The convective phase of the MJO has been shown to be associated with enhanced activity of high-frequency disturbances (Nakazawa 1986; Yamazaki and Murakami 1989; Sui and Lau 1992; Straub and Kiladis 2003). Sobel and Maloney (2000) computed barotropic wave activity flux divergence for different phases of the MJO and showed that accumulation of wave energy was favored when the MJO was convectively active. These results indicate that the MJO environment provides conditions that may be favorable for the growth and transformation of MRG waves. It is important to understand the role of the MJO in the development of off-equatorial disturbances since they are often observed to be precursors to tropical cyclones in the western Pacific (e.g., Takayabu and Nitta 1993). As recognized by Sobel and Bretherton (1999), the transition from an MRG wave to a TD-type disturbance is a complex phenomenon that involves reduction in the wavelength of the MRG wave and the elimination of the symmetric structure of the MRG wave. However, the process by which such an evolution occurs is not yet well understood.

In the present study, we employ a simple numerical model to simulate the evolution of the MRG waves in environments representative of the MJO in the western Pacific. Idealized models have been used in the past to study problems similar to the one addressed in this study (e.g., Kuo et al. 2001; Hartmann and Maloney 2001). The approach taken in the present study is that of an initial value problem wherein a preexisting MRG wave is introduced in an environment taken to represent the MJO. Here, the MJO is defined as the steady-state response of the tropical atmosphere to localized heating and frictional damping. In the model, a mass sink serves as a proxy for convective heating. Such a methodology has been used in previous studies to simulate the effect of tropical heating in general (e.g., Gill 1980; Zhang and Krishnamurti 1996), as well as the MJO (e.g., Yamagata and Hayashi 1984; Ferreira et al. 1996). The MJO circulation thus obtained is prescribed to be the

time-invariant basic state within which the MRG wave is allowed to evolve. The initial structure of the MRG wave is derived analytically. The goals of the numerical simulation are to study the amplification of MRG waves within the convective envelope of the MJO and to simulate the development of TD-type off-equatorial disturbances.

## 2. The shallow water equations

The governing equations for a single homogeneous layer of fluid on an  $\beta$  plane are

$$\frac{du}{dt} - \beta yv = -g \frac{\partial h}{\partial x} + F_x, \quad (1)$$

$$\frac{dv}{dt} + \beta yu = -g \frac{\partial h}{\partial y} + F_y, \quad (2)$$

$$\frac{dh}{dt} + h \left( \frac{\partial u}{\partial x} + \frac{\partial v}{\partial y} \right) = F_h, \quad (3)$$

where  $u$  and  $v$  are the Cartesian components of fluid velocity,  $h$  is the free surface height,  $\beta$  is the meridional gradient of the Coriolis parameter, and  $g$  is the acceleration due to gravity;  $F_x$ ,  $F_y$ , and  $F_h$  represent forcing by physical mechanisms that will be specified later.

We separate the flow field into a time-invariant basic state and a perturbation state such that

$$\begin{aligned} u(x, y, t) &= \bar{u}(x, y) + u'(x, y, t), \\ v(x, y, t) &= \bar{v}(x, y) + v'(x, y, t), \\ h(x, y, t) &= \bar{h}(x, y) + h'(x, y, t) + H, \\ F_{x,y,h} &= \bar{F}_{x,y,h}, \end{aligned} \quad (4)$$

where the terms with overbars denote the time-invariant basic-state fields, the terms with primes are the perturbation fields, and  $H$  is the mean layer depth of the undisturbed fluid.

After expressions in (4) are substituted in Eqs. (1)–(3) and the nonlinear terms are neglected (as in Gill 1980; Yamagata and Hayashi 1984; Zhang and Krishnamurti 1996), a balance among the terms of the leading order yields the following set of equations for the basic state:

$$-\beta y \bar{v} = -g \frac{\partial \bar{h}}{\partial x} + \bar{F}_x, \quad (5)$$

$$\beta y \bar{u} = -g \frac{\partial \bar{h}}{\partial y} + \bar{F}_y, \quad (6)$$

$$H \frac{\partial \bar{u}}{\partial x} + H \frac{\partial \bar{v}}{\partial y} = \bar{F}_h, \quad (7)$$

while a balance between the higher-order terms, after neglecting the nonlinear terms, leads us to the equations for the perturbation state given by

$$\begin{aligned} \frac{\partial u'}{\partial t} + \bar{u} \frac{\partial u'}{\partial x} + u' \frac{\partial \bar{u}}{\partial x} + \bar{v} \frac{\partial u'}{\partial y} + v' \frac{\partial \bar{u}}{\partial y} - \beta y v' \\ = -g \frac{\partial h'}{\partial x}, \end{aligned} \quad (8)$$

$$\begin{aligned} \frac{\partial v'}{\partial t} + \bar{u} \frac{\partial v'}{\partial x} + u' \frac{\partial \bar{v}}{\partial x} + \bar{v} \frac{\partial v'}{\partial y} + v' \frac{\partial \bar{v}}{\partial y} + \beta y u' \\ = -g \frac{\partial h'}{\partial y}, \end{aligned} \quad (9)$$

$$\begin{aligned} \frac{\partial h'}{\partial t} + \frac{\partial}{\partial x} [(\bar{h} + H)u' + h'\bar{u}] + \frac{\partial}{\partial y} [(\bar{h} + H)v' + h'\bar{v}] \\ = 0. \end{aligned} \quad (10)$$

As evident from (5)–(7), the forcing terms  $F_x$ ,  $F_y$ , and  $F_h$  are specified to maintain a steady basic state. On the other hand, equations for the perturbations (8)–(10) do not contain any forcing terms. In this regard, our approach is similar to the method used in several past studies (e.g., Shapiro 1980; Kuo et al. 2001). The shallow water equations are cast in finite differences form and integrated on an equatorial  $\beta$  plane that is periodic along the zonal direction and confined within a channel along the meridional direction. The zonal extent of the domain is 40 000 km, which is roughly the circumference of the earth along the equator. The meridional extent is 8000 km. A uniform grid spacing of 50 km and a time step of 600 s are used for all simulations described here. A leapfrog scheme with a time filter that damps high-frequency waves is employed to carry out the model integration.

The mean fluid depth in the shallow water model is set at 25 m. The rationale for choosing this value is based on the implied equivalent depths of equatorial waves that have been detected in observations. Liebmann and Hendon (1990) identified lower-tropospheric MRG waves through spectral analysis of winds and found that their equivalent depths ranged from 1–60 m. Wheeler and Kiladis (1999) noted that the equivalent depths of convectively coupled equatorial waves typically lie in the 12–50-m range. In their case study, Dickinson and Molinari (2002) found that the best theoretical fit for the phase and group speeds of the MRG wave observed by them implied equivalent depths of 10 to 25 m. As discussed in Wheeler and Kiladis (1999), equivalent depths of waves that are coupled to convection (i.e., ones that force wave-scale convection) are much smaller than those that are not coupled to convection. By choosing an equivalent depth of 25 m in our simulations, we effectively consider those MRG waves that would be coupled with convection in nature. However, the results of the simulations presented here are not sensitive to the choice of the equivalent depth. The outcomes of the simulations were qualitatively similar when values of 50 and 200 m were used.

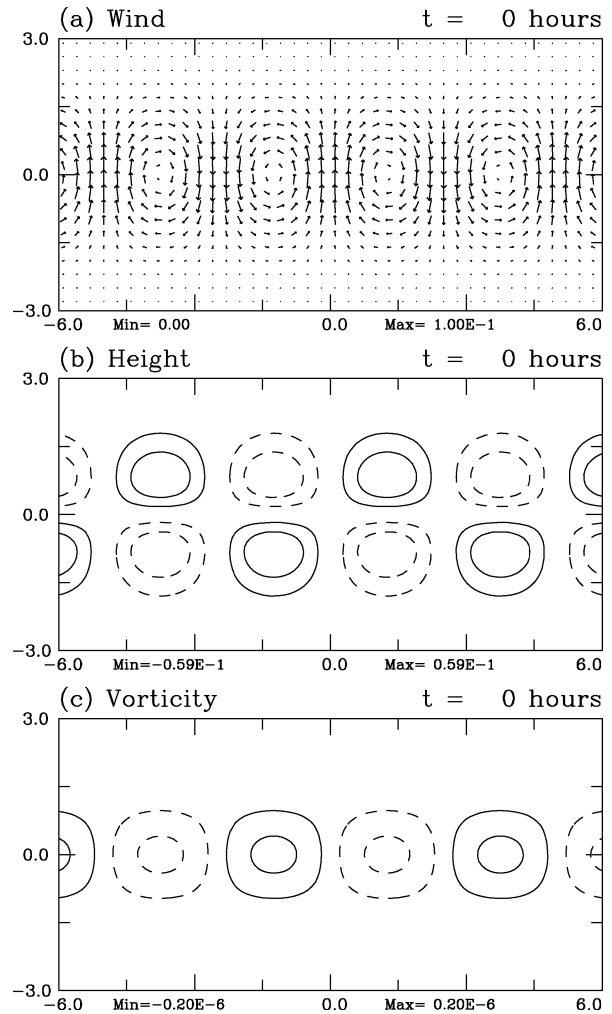


FIG. 1. Fields associated with the wavenumber-8 MRG wave in an equatorial  $\beta$  plane: (a) wind (maximum vector shown is  $0.1 \text{ m s}^{-1}$ ), (b) height (contour interval  $0.02 \text{ m}$ ), and (c) relative vorticity (contours shown are  $\pm\{0.05, 0.16\} \times 10^{-6} \text{ s}^{-1}$ ). Dashed contours denote negative values. Domain shown is  $12\,000 \text{ km} \times 6\,000 \text{ km}$ .

### 3. MRG waves in an equatorial $\beta$ -plane channel

To derive the structures of the initial MRG wave, we follow the method outlined by Zehnder (1991), with the exception that we retain the dimensional form of all variables (see appendix A for details). The vector winds, perturbation height, and vorticity associated with the wavenumber-8 MRG mode confined to a channel are shown in Fig. 1. The amplitude of the MRG wave is chosen such that conditions for linearizing the flow about a basic state assumed in Eqs. (8)–(10) are satisfied throughout the course of the simulations presented here. The maximum wind speed of  $0.1 \text{ m s}^{-1}$  associated with this wave occurs at the equator in the meridional component of the wind. The maximum perturbations in the height and vorticity associated with the wave are, respectively,  $0.06 \text{ m}$  and  $2 \times 10^{-7} \text{ s}^{-1}$ . The wave period is about 6.3 days.

#### 4. The MJO basic state

The steady-state response of the tropical atmosphere to localized heating and frictional damping is used to define the MJO environment. In the shallow water model, the effect of lower-tropospheric heating is simulated by a mass sink. Thus, in our idealized framework, the mass sink is a proxy for the convective signal associated with the active phase of the MJO.

The large-scale response of the tropical atmosphere to local forcing has received considerable attention in the past. Matsuno (1966) studied the forced motion of a homogeneous layer of fluid subject to a series of mass sources and sinks. Webster (1972) used a two-layer model with an imposed distribution of heating to simulate some of the observed features in the mean state of the equatorial atmosphere. Analytic solutions for steady-state flow in response to heating in the presence of Rayleigh friction and Newtonian cooling were obtained by Gill (1980). In his study, Gill (1980) investigated the response of idealized heating distributions (symmetric as well as asymmetric about the equator) and interpreted the results within a framework of stationary Kelvin and planetary-scale Rossby waves. Several past studies have used a mass sink to simulate the MJO in an idealized numerical model (e.g., Yamagata and Hayashi 1984; Ferreira et al. 1996). In the remainder of this section, we will discuss the procedure used to derive the MJO basic states.

The basic-state fields are obtained by integrating the shallow water equations, starting from rest, until a steady state is reached in response to a mass sink that is in balance with specified damping. The relevant equations are (5)–(7), which, after specifying the forcing terms, are written as

$$-\beta y \bar{v} = -g \frac{\partial \bar{h}}{\partial x} - \alpha \bar{u}, \quad (11)$$

$$\beta y \bar{u} = -g \frac{\partial \bar{h}}{\partial y} - \alpha \bar{v}, \quad (12)$$

$$H \frac{\partial \bar{u}}{\partial x} + H \frac{\partial \bar{v}}{\partial y} = m - \gamma \bar{h}, \quad (13)$$

where  $\alpha$  and  $\gamma$ , respectively, represent Rayleigh friction and Newtonian cooling (Gill 1980), and  $m$  denotes the mass sink. As in past studies (Yamagata and Hayashi 1984; Ferreira et al. 1996), for the sake of retaining the simplicity of the approach, no momentum source is specified in association with the mass forcing. Both parameters  $\alpha$  and  $\gamma$  are set to correspond to an  $e$ -folding timescale of 5 days. A period of 40 days is found to be sufficient to achieve a steady state for the configuration specified in this study. The results were qualitatively similar when  $e$ -folding timescales of 3 and 10 days were considered (not shown). By choosing different strengths and structures of the mass sink, we can change the structure of the basic state. In this study, we examine

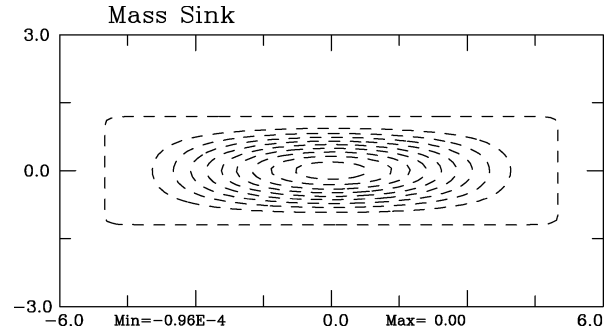


FIG. 2. Mass sink (contour interval  $0.1 \times 10^{-4} \text{ m s}^{-1}$ ) used to create the B1 (symmetric) basic state. Dashed contours denote negative values. Domain shown is  $12\,000 \text{ km} \times 6\,000 \text{ km}$ .

the evolution of MRG waves in two different basic states.

The mass sink structure used to obtain the first basic state (henceforth referred to as the B1 or the symmetric basic state) is given by

$$m = m_0 \left[ 1 + \cos\left(\frac{\pi x}{x_0}\right) \right] \left[ 1 + \cos\left(\frac{\pi y}{2y_0}\right) \right], \quad (14)$$

where  $m_0 = -2.4 \times 10^{-6} \text{ m s}^{-1}$ ,  $x_0 = 5 \times 10^6 \text{ m}$ , and  $y_0 = (c/2\beta)^{1/2}$  is the equatorial Rossby radius of deformation. The mass sink is placed at the center of the domain, and is symmetric about the equator (Fig. 2). The amplitude of the mass sink is maximum at the equator. The steady-state fields resulting from this forcing are shown in Fig. 3. The prominent feature of the solution is the difference in the structure on either side of the mass sink. The steady state is interpreted as being a combination of a Rossby mode west of the mass forcing and a Kelvin mode east of the forcing (Matsuno 1966; Gill 1980). The zonal flow at the equator reverses direction at around  $x = 1500 \text{ km}$  (Fig. 3b). The chosen strength of the mass sink yields a steady-state convergence (Fig. 3c) on the order of  $10^{-6} \text{ s}^{-1}$ , which is similar to the value used by Hartmann and Maloney (2001). The region of convergence extends from about  $x = -4000 \text{ km}$  to  $x = 4000 \text{ km}$  and is flanked on either side by weak divergence. The steady state is similar to the solution described by Gill (1980), except that all the fields are zonally elongated in response to the broad mass sink shown in Fig. 2.

As seen in Fig. 3, the B1 basic state is symmetric about the equator—a result of choosing a symmetric mass sink. Observations indicate that the convective signal associated with the MJO is often maximum not at the equator but on one side of the equator. To examine the evolution of the MRG waves in a relatively more realistic MJO environment, we also consider a mass sink that is asymmetric about the equator. The mass sink depicted in Fig. 4 was obtained by translating the one shown in Fig. 2 meridionally by  $1000 \text{ km}$  and then rotating it clockwise by  $20^\circ$ . This mass sink is an idealization of the convection associated with an active

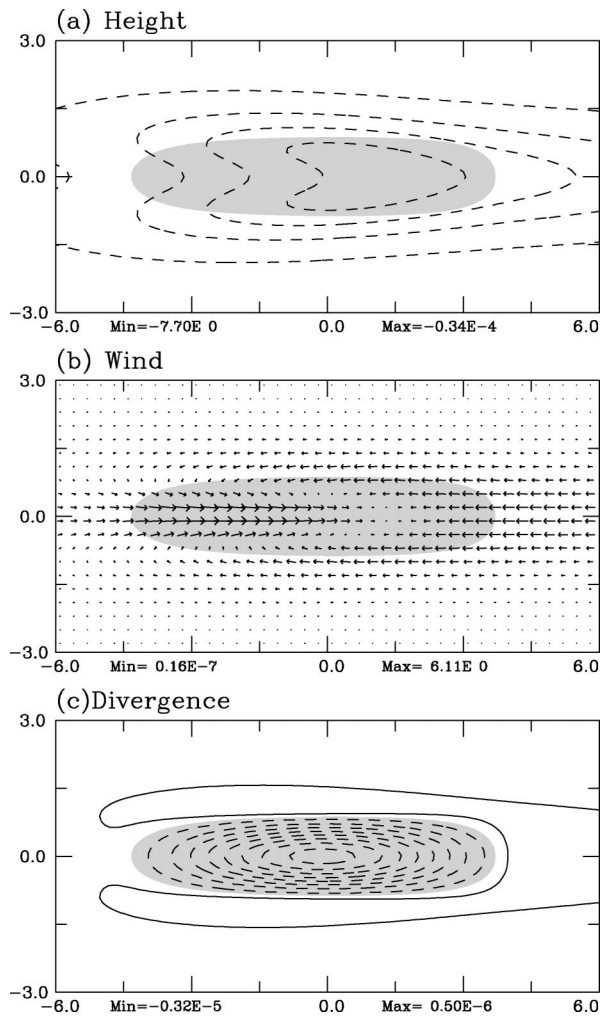


FIG. 3. Steady-state fields associated with the B1 (symmetric) basic state. (a) Height (contour interval 2.0 m), (b) wind (maximum vector shown is  $6.1 \text{ m s}^{-1}$ ), and (c) divergence (contour interval  $0.4 \times 10^{-6} \text{ s}^{-1}$ ). The shaded region in each denotes basic-state convergence.

MJO event examined by Dickinson and Molinari (2002, their Figs. 4c and 5). A similar signal can also be seen in the composite OLR associated with strong MJO events over the western Pacific studied by Maloney and Hartmann (2001).

The steady-state solution to the asymmetric mass sink is shown in Fig. 5 (henceforth referred to as the B2 or the asymmetric basic state). While the structure bears some of the characteristics seen in Fig. 3, the steady state exhibits a prominent asymmetry about the equator. In particular, the response in the Northern Hemisphere, where the bulk of the heating is specified, is stronger than its Southern Hemisphere counterpart. In the Northern Hemisphere, west of the mass sink center, a distinct cyclonic gyre can be seen. A broad trough comprises the solutions to east of the mass sink. The Rossby mode, west of the mass forcing, is considerably more asymmetric than the Kelvin mode, east of the forcing. In this

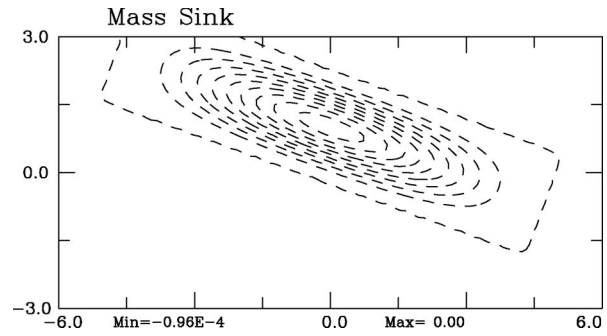


FIG. 4. As in Fig. 2, except for B2 (asymmetric) basic state.

case, the zonal flow at the equator changes from westerly to easterly at around  $x = 2000 \text{ km}$  (Fig. 5b). At the equator, the region of convergence extends from about  $x = 0 \text{ km}$  to  $x = 4000 \text{ km}$  beyond which, on either side, weak divergence is observed (Fig. 5c). Several past studies (e.g., Gill 1980; Heckley and Gill 1984) have

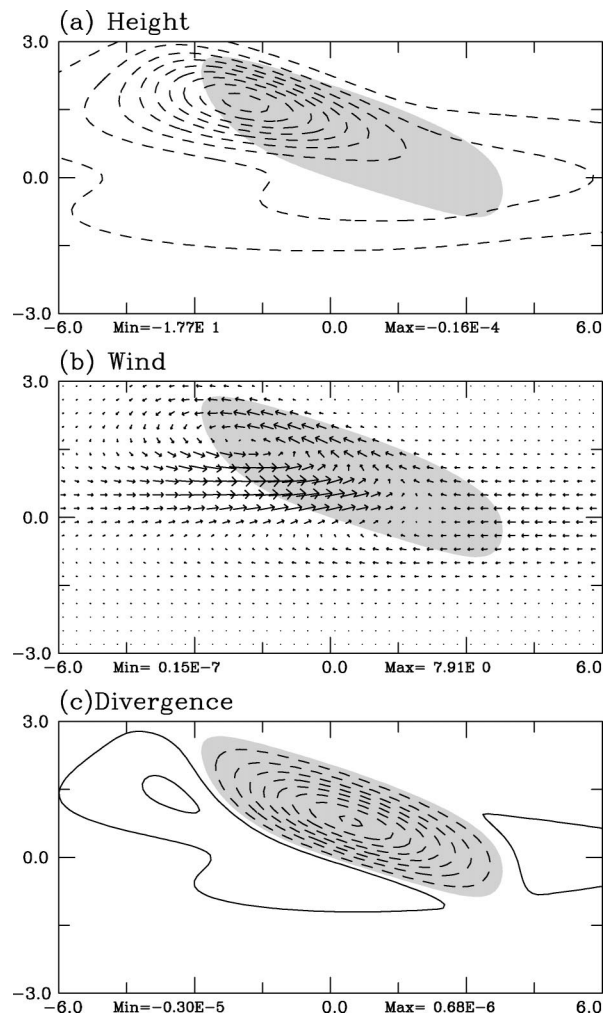


FIG. 5. As in Fig. 3, except for B2 (asymmetric) basic state.

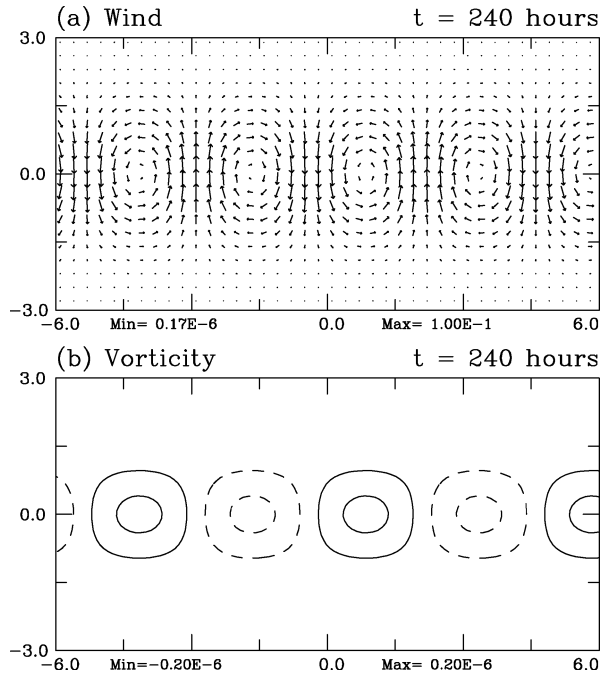


FIG. 6. Charts of (a) wind vectors and (b) relative vorticity ( $s^{-1}$ ) associated with the MRG wave in a quiescent environment after  $t = 240$  h. Vector size and contour interval same as in Fig 1.

are inhomogeneous in space, but are invariant in time. As seen in Figs. 3 and 5, these two basic states exhibit a reversal in the zonal wind direction at the equator. Several studies in the past have examined the influence of opposing background zonal flow on wave propagation (Farrel and Watterson 1985; Webster and Chang 1988; Sobel and Bretherton 1999; Kuo et al. 2001). These studies have shown that reversal in the environmental zonal flow can lead to accumulation of wave energy through scale contraction of the wave and convergence of group velocity. The same problem was also studied by Shapiro (1977) in relation to development of tropical cyclones from easterly waves. The presence of opposing background zonal flow in B1 and B2 basic states is expected to play an important role in the evolution of the MRG wave near the equator.

**5. Evolution of MRG waves in MJO-type environments**

Before we examine the influence of the MJO environment on the MRG wave, we perform a control simulation in which the MRG wave is allowed to evolve in a quiescent environment. The wind and vorticity fields after 240 h of simulation are shown in Fig. 6. Comparing Figs. 1 and 6, it can be seen that the wave has propagated westward without any change in its structure. The Hovmöller diagram of the meridional wind at equator for this simulation is shown in Fig. 7. From the slope of the phase lines the westward phase speed is estimated to be  $9 \text{ m s}^{-1}$ , consistent with the theoretical phase speed for this wave. Figure 8 depicts

examined the response to an asymmetric mass sink and the results in Fig. 5 are consistent with their findings.

The two basic states described above are taken to represent the idealized MJO environments within which the MRG waves are allowed to evolve. Both B1 and B2

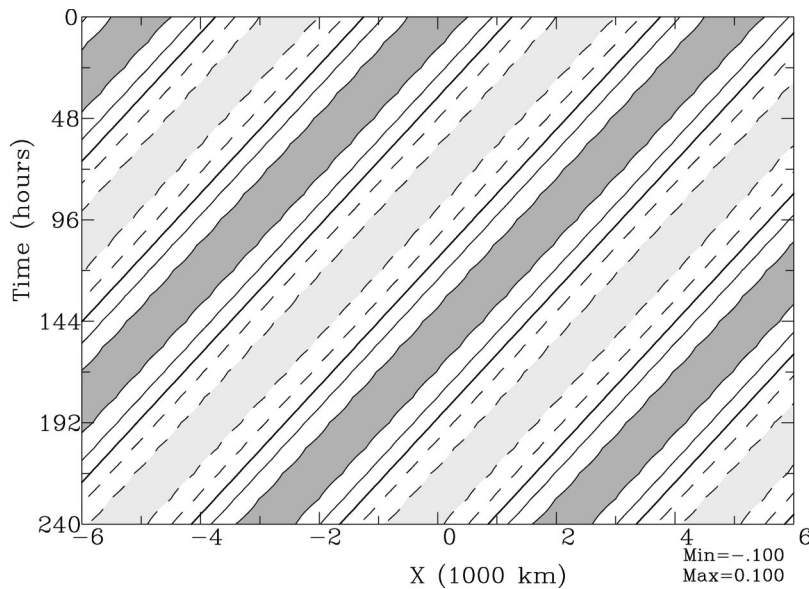


FIG. 7. The Hovmöller diagram of meridional wind ( $m s^{-1}$ ) at the equator for the evolution of the MRG wave in a quiescent environment. Contour interval is  $0.04 \text{ m s}^{-1}$  with dark shading for values greater than  $0.08 \text{ m s}^{-1}$  and light shading for values less than  $-0.08 \text{ m s}^{-1}$ .

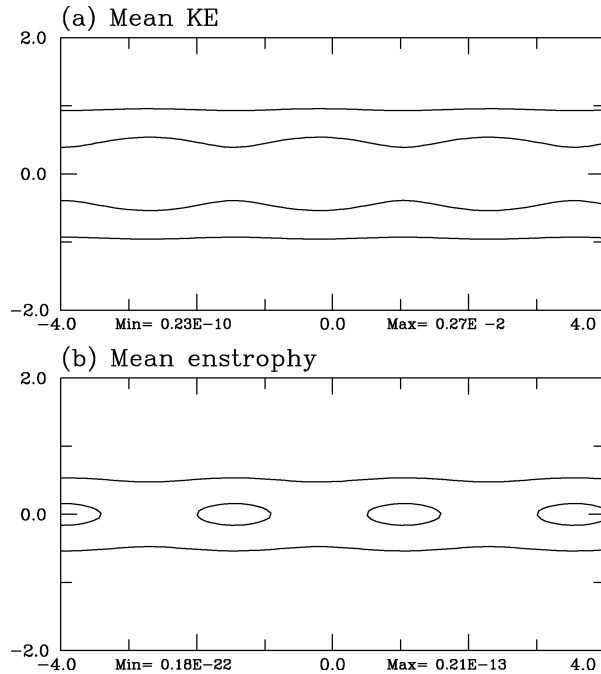


FIG. 8. (a) Perturbation kinetic energy (contour interval of  $0.1 \times 10^{-2} \text{ m}^2 \text{ s}^{-2}$ ), and (b) enstrophy (contour interval of  $10^{-14} \text{ s}^{-2}$ ), each averaged over 240 h of simulation of the MRG wave in a quiescent environment. Domain shown is  $8000 \text{ km} \times 4000 \text{ km}$ .

the kinetic energy and enstrophy, each averaged over 240 h of simulation. In a quiescent environment, the mean kinetic energy and enstrophy are nearly zonally symmetric, with maximum values occurring at the equator.

#### a. Symmetric basic state

We now consider the evolution of the MRG wave in the B1 basic state. Figure 9a shows the wind and relative vorticity fields at the initial time. The shaded region represents the convergence field of the MJO environment. At 0 h, the convergence associated with the B1 basic state spans a distance of approximately two wavelengths along the zonal direction. From the subsequent development shown in the remaining panels of Fig. 9, it is readily apparent that the MJO background significantly alters the structure of the MRG wave. After 120 h (Fig. 9b), the section of the wave labeled “A” that was located at around  $x = 3500 \text{ km}$  at the initial time has propagated into the region of background convergence and is approaching the location where the background zonal flow reverses direction. It is evident from the magnitude of the wind vectors as well as the vorticity (Fig. 9b) that the MRG wave has amplified under the envelope of the basic-state convergence. The evolution of “B,” the circulation center of opposite sign that follows A, is similar. The spacing between the circulation centers A and B at 120 h has decreased considerably from its initial value. This indicates that the zonal scale

of the MRG wave has reduced in response to the influence of the environmental flow. In addition, both A and B have been deformed by the background shear. The initially circular features have now acquired a down-shear tilt on either side of the equator. After 180 h, the circulation center A has moved well to the west of the point of zonal flow reversal while B is in the vicinity of that point. By 240 h, A has reached the western boundary of the convergent region and has partly recovered its initial MRG structure.

The Hovmöller diagram of the meridional wind at the equator (Fig. 10) provides us with another perspective to examine the evolution described above. When compared to Fig. 7, several features of interest are evident, prominent among them being the larger wave amplitude, a decrease in the phase speed of the MRG wave in the vicinity of the zonal flow reversal, and the development of a wave packet that first appears on the western side of the background convergence. The wave packet forms as a result of the amplification of the part of the MRG wave that moves into the region of background convergence. As inferred from the slope of the line joining the maxima and minima in the Hovmöller diagram, the wave packet is associated with an eastward group speed. We also note a reduction in the group speed as the wave packet approaches  $x = 1500 \text{ km}$ . This is a consequence of the reversal in the zonal background flow in this region. The background winds east of  $x = 1500 \text{ km}$  are in opposite direction to the eastward-moving wave packet and thus oppose its propagation.

It is of interest to understand the process by which the vorticity associated with the MRG wave amplifies as it evolves within the B1 basic state. An equation for the eddy vorticity, constructed from (8)–(10), can be written as

$$\frac{\partial \zeta'}{\partial t} = -\mathbf{v}' \cdot \nabla \bar{\zeta} - \beta v' - \bar{\mathbf{v}} \cdot \nabla \zeta' - (\bar{\zeta} + \beta y) D' - \zeta' \bar{D}, \quad (15)$$

where  $\mathbf{v}'$ ,  $D'$ , and  $\zeta'$  ( $\bar{\mathbf{v}}$ ,  $\bar{D}$ , and  $\bar{\zeta}$ ) are, respectively, the vector wind, divergence, and vorticity for the perturbations (basic state). The first three terms on the rhs represent local vorticity tendency due to advective effects. The fourth term,  $-(\bar{\zeta} + \beta y) D'$ , represents vorticity change due to convergence within a background with nonzero absolute vorticity. In a background characterized by positive absolute vorticity, disturbance scale convergence leads to amplification of positive perturbation vorticity and decay of negative perturbation vorticity. The fifth term,  $-\zeta' \bar{D}$ , implies that within a region of background convergence (i.e.,  $\bar{D} < 0$ ), perturbation vorticity can amplify irrespective of its sign.

The terms of the perturbation vorticity equation (15) will be averaged over 240 h of the simulation. The reader is reminded that the bar indicates the time-invariant background flow. The primed fields are not deviations from a time mean, but rather are perturbations that grow

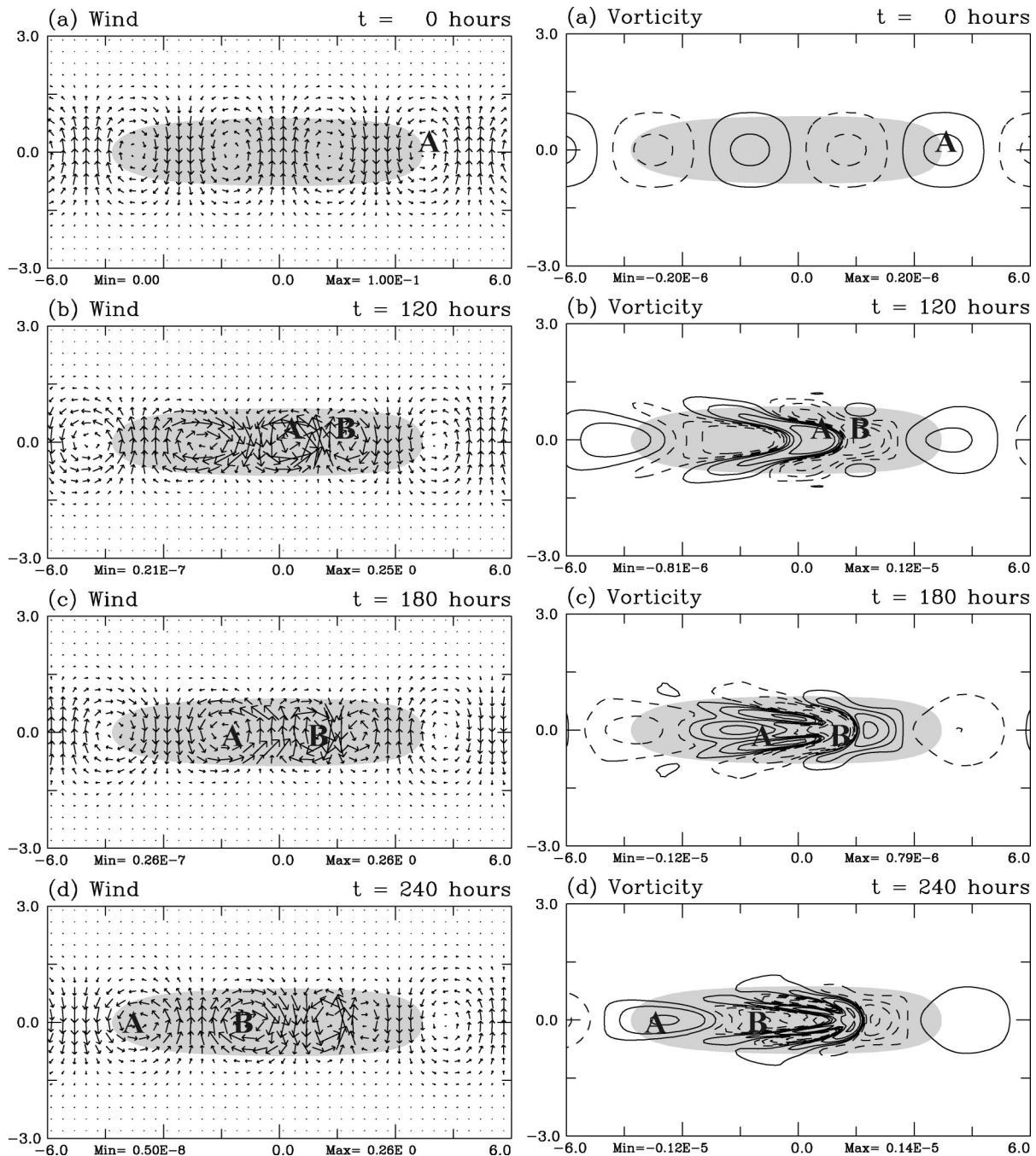


FIG. 9. Charts of wind vectors (maximum vector shown is  $0.26 \text{ m s}^{-1}$ ) and relative vorticity (contours shown are  $\pm 0.05, 0.16, 0.32, 0.64,$  and  $1.28 \times 10^{-6} \text{ s}^{-1}$ ) associated with the evolution of the MRG wave in the B1 (symmetric) basic state after (a)  $t = 0$  h, (b)  $t = 120$  h, (c)  $t = 180$  h, and (d)  $t = 240$  h. The shaded area denotes basic-state convergence. Domain shown is  $12\,000 \text{ km} \times 6000 \text{ km}$ .

and decay, via Eqs. (8)–(10) in the presence of nonzero background fields associated with the mass sink forcing. In the absence of the mass sink, the initial MRG waves would not change structure and would have a time mean at any given grid point of almost zero (exactly zero if the averaging period is a multiple of the wave period). With a nonzero mass sink, the perturbation fields will

have a nonzero time mean as a result of convergence or divergence of the background and energy exchanges with the background. In the text to follow, the time-mean perturbation vorticity that results will sometimes be labeled the “mean vorticity.” The same terminology will hold for other perturbation quantities such as kinetic energy.

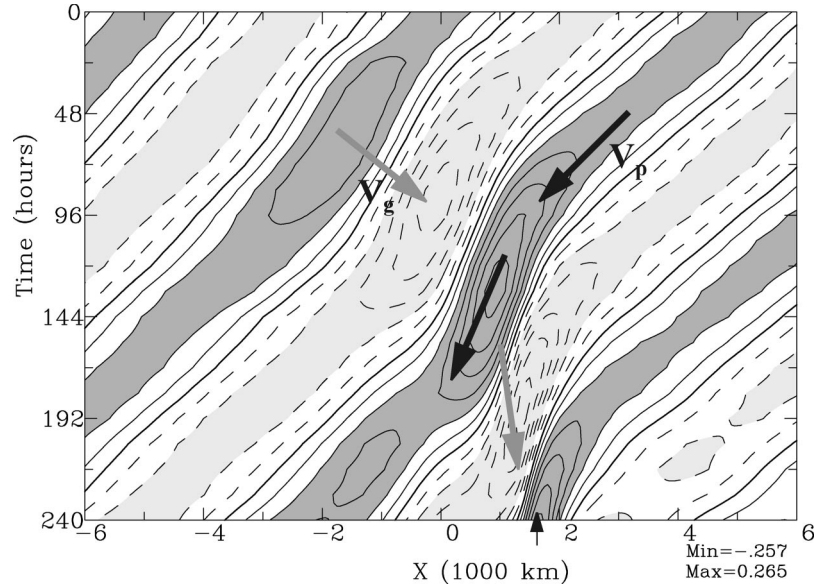


FIG. 10. As in Fig. 7 except for the evolution of the MRG wave in the B1 (symmetric) basic state. Thick gray and black arrows represent, respectively, the group and phase directions. The thin vertical arrow on the  $x$  axis marks the point of reversal of background zonal wind.

Charts of vorticity and the two nonadvective forcing terms in (15), each averaged over 240 h of the simulation, are presented in Fig. 11. The main feature of interest in Fig. 11a is the nonzero mean vorticity within the region of basic-state convergence indicating local growth of the MRG wave. From Figs. 11b and 11c we note the term  $-\zeta'D$  dominates the vorticity tendency. This highlights the role of the convergence in the background in the amplification of the MRG wave.

An integral component of the convergence in the basic state is the reversal of the zonal flow from westerly to easterly around  $x = 1500$  km at the equator. From Figs. 9 and 10 it was noted that within the convergent background, the MRG wavelength experienced a contraction while a wave packet developed. Furthermore, the motion of the wave packet was opposed by the background while it moved eastward across the region of reversal in the zonal flow (Fig. 10). This behavior is consistent with the process of energy accumulation, which occurs as a result of slow down of the group speed of a wave packet (e.g., Webster and Chang 1988; Sobel and Bretherton 1999). Kuo et al. (2001) showed that in addition to background confluence that leads to scale contraction, the presence of background convergence was crucial for accumulation of Rossby wave energy. The MJO basic state considered here provides both ingredients and consequently leads to the local growth of the MRG wave. The mean kinetic energy and enstrophy for the symmetric heating simulation are shown in Fig. 12. Comparing Fig. 8 and Fig. 12, we note that there is a net accumulation of eddy kinetic energy as well as enstrophy within the MJO background.

Although off-equatorial parts of the wave amplify

within the region of background convergence, the maximum amplitude of the wave is always located at the equator, consistent with the initial structure of the MRG wave. The results of this simulation suggest that MJO backgrounds symmetric about the equator may allow MRG waves to grow, but may not be instrumental in developing smaller-scale off-equatorial circulations such as the TD-type disturbances.

#### b. Asymmetric basic state

We consider next the B2 basic state, which is asymmetric about the equator. As discussed earlier, this basic state is an idealization of the active MJO event examined by Dickinson and Molinari (2002). The wind and vorticity fields at various stages of the simulation for this case are illustrated in Fig. 13. As before, the basic-state convergence is shaded for reference. At the initial time, the circulation center labeled A is located immediately east of the basic-state convergence. After 120 h (Fig. 13b), A has crossed the point of reversal in the zonal background flow ( $x = 2000$  km) and has amplified considerably from its initial strength. It is also notable that the maximum vorticity associated with A is no longer at the equator, but is approximately 300 km north of the equator, indicating an apparent northward shift of the MRG wave. Also evident in Fig. 13b are the small-scale eddies that have developed within the envelope of convergence further to the north of A. These eddies have their origin in parts of the MRG wave that preceded A during the first 120 h of simulation and moved within the MJO background (not shown). These features become more prominent as the simulation proceeds.

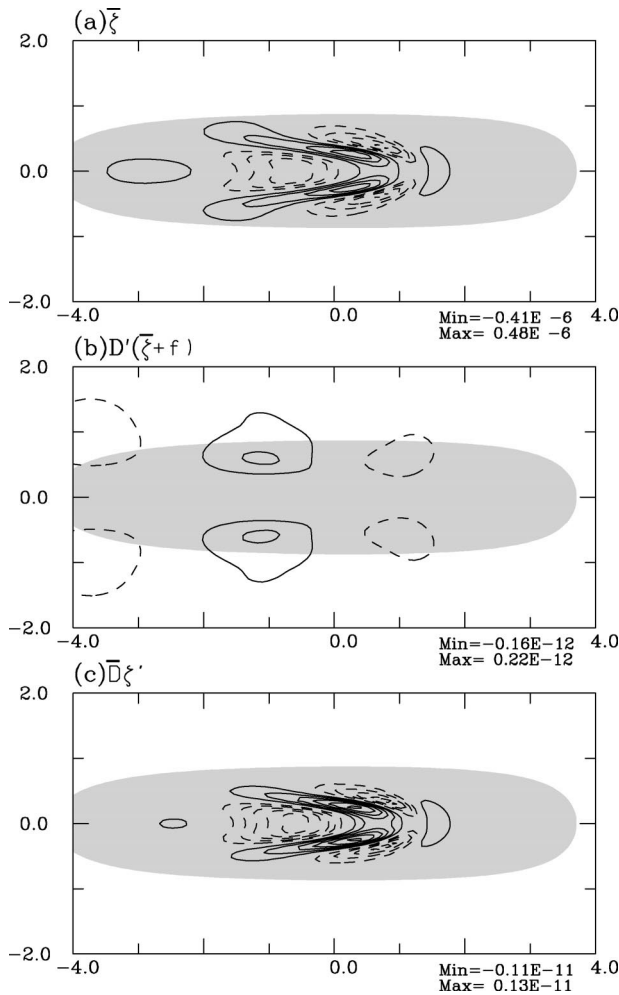


FIG. 11. Charts of (a) vorticity (contour interval of  $1 \times 10^{-7} \text{ s}^{-1}$ ), (b)  $D'(\bar{\zeta} + f)$  (contour interval of  $1 \times 10^{-13} \text{ s}^{-2}$ ), and (c)  $\bar{D}\zeta'$  (contour interval of  $2 \times 10^{-13} \text{ s}^{-2}$ ), each averaged over the 240 h of simulation of the MRG wave in B1 (symmetric) basic state. Domain shown is  $8000 \text{ km} \times 4000 \text{ km}$ .

After 180 h (Fig. 13c), the circulation A appears to have two components, one that is emerging out of the background convergence along the equator and another that is north of the equator. The latter part of A is much smaller in scale and remains under the convergent envelope of the MJO environment. Indeed, after 240 h of the simulation (Fig. 13d), the two components have separated. The original circulation A is now well west of the background convergence, while the circulation feature that developed from it, now labeled “a,” remains within the background convergence and continues to amplify and move slowly to the northwest. As seen clearly in the wind vectors and the relative vorticity fields, a series of small-scale eddies oriented along a northwest to southeast axis has resulted.

Figure 14 is a close-up of the height fields associated with the eddies seen in Fig. 13d. With length scales of 1000–2000 km, they are smaller than the initial MRG

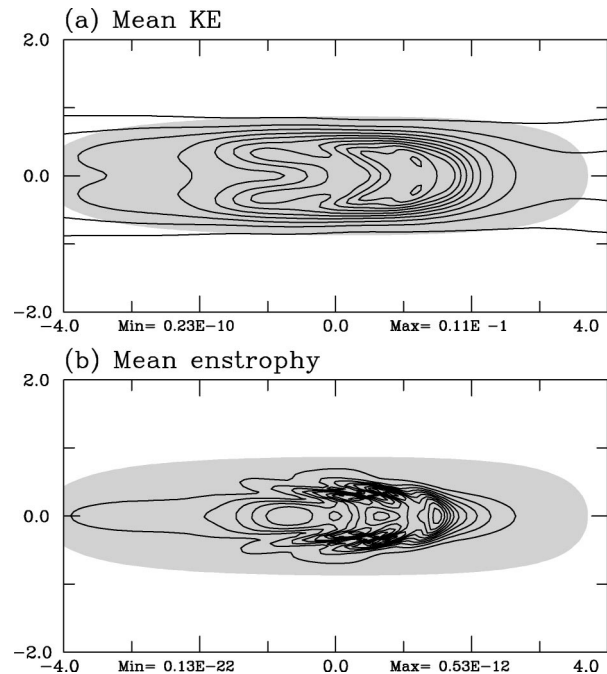


FIG. 12. (a) Perturbation kinetic energy (contour interval of  $0.1 \times 10^{-2} \text{ m}^2 \text{ s}^{-2}$ ) and (b) enstrophy (contour interval of  $5 \times 10^{-14} \text{ s}^{-2}$ ), each averaged over 240 h of simulation of the MRG wave in a quiescent environment. Domain shown is  $8000 \text{ km} \times 4000 \text{ km}$ .

waves and since the circulations are located entirely within the Northern Hemisphere, we can identify them as cyclonic and anticyclonic disturbances. Their motion is directed toward the northwest with a speed that is much smaller than the phase speed of the parent MRG wave. Their alignment and motion is related to the basic-state flow field. Comparing Figs. 5 and 14b, it can be seen that the eddies are embedded within the northwestward flow of the basic-state gyre. The eddies move at approximately  $1\text{--}2 \text{ m s}^{-1}$  and are aligned along the basic-state flow. However, the basic-state winds in this region vary between  $2\text{--}4 \text{ m s}^{-1}$ , indicating that the eddies are not merely being advected by the background flow. The eddies might be behaving like MRG waves with group propagation that opposes the advection by the basic state, even though they are well away from the equator. In support of this, it is found that the eddy vorticity and divergence fields are in quadrature (not shown), consistent with the original MRG wave structure. It is likely that, in a similar situation in nature, Ekman pumping would eventually induce wave-scale convection within the cyclonic disturbances and bring the eddy vorticity and convergence in phase.

The results shown in Figs. 13 and 14 suggest that when the MRG wave is placed in the B2 basic state, individual circulation centers associated with the wave amplify, and parts of them evolve into smaller-scale eddies. From Fig. 13, it can be noted that there are two aspects to the evolution of the MRG wave in the asymmetric MJO environment. One of them is the off-equa-

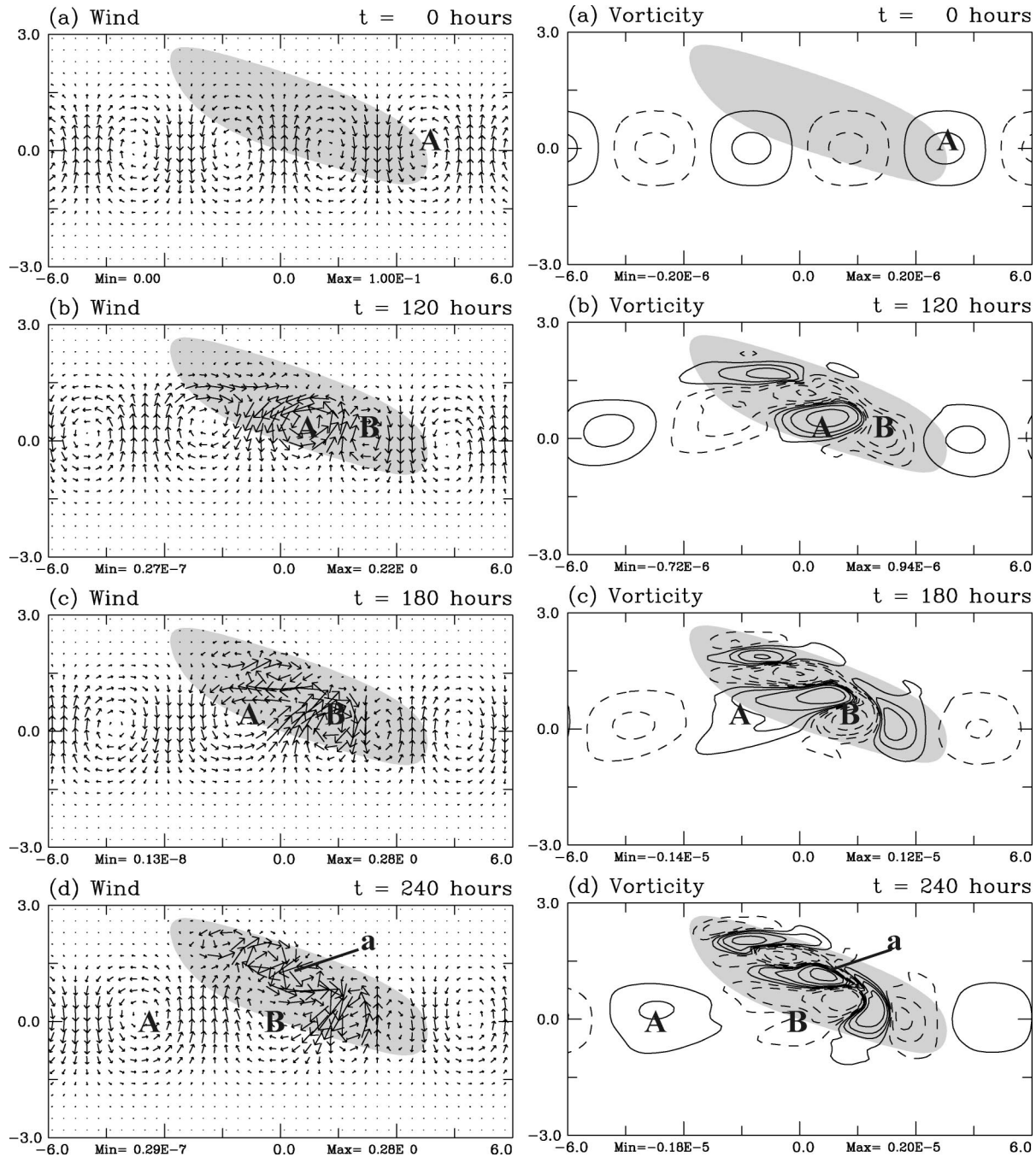


FIG. 13. As in Fig. 9, except for the evolution of the MRG wave in the B2 (asymmetric) basic state. The shaded area denotes basic-state convergence. Domain shown is  $12\,000\text{ km} \times 6000\text{ km}$ .

torial development described above. In addition, the fields in Fig. 13 exhibit some of the behavior seen in the simulation with the B1 environment (Fig. 9). A comparison of Figs. 13a and 13b shows that the wavelength of the MRG wave has decreased in the vicinity of the opposing background zonal flow ( $x = 2000\text{ km}$ ). The near-equatorial parts of the wave within the convergent background have also amplified from their initial

strength. Figure 15 depicts the Hovmöller diagram for the meridional wind at the equator for this simulation. As in the case with the B1 basic state (Fig. 10), the development of a wave packet is evident. The eastward motion of the packet is retarded as the packet moves towards  $x = 2000\text{ km}$ , where the zonal flow at the equator changes from westerly to easterly. The amplification of the wave at the equator is also evident in

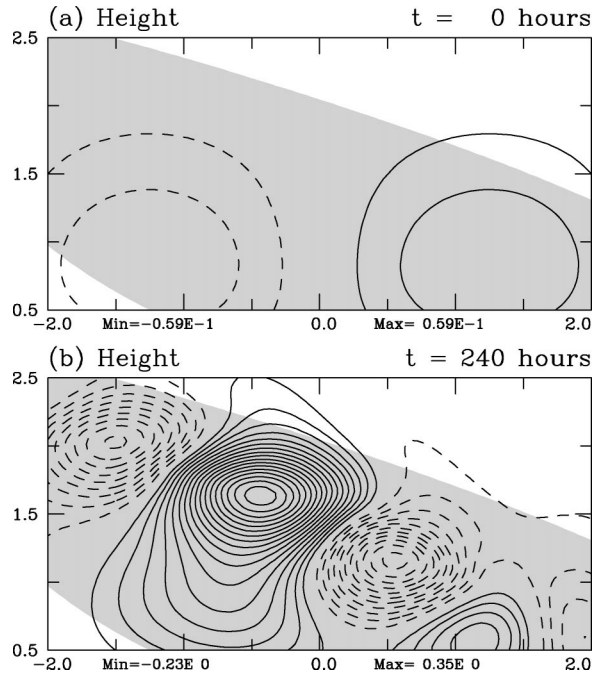


FIG. 14. Close-up view of the height field (contour interval 0.02 m) for the evolution of the MRG wave in the B2 (asymmetric) basic state after (a) 0 h and (b) 240 h. The shaded area denotes basic-state convergence. Domain shown is 4000 km × 3000 km.

Fig. 15. Thus, as in the previous simulation, wave accumulation appears to be playing a role in the growth of the MRG wave near the equator.

The time-mean perturbation vorticity and the contributions of the two nonadvective terms in (15) for this simulation are shown in Fig. 16. As in Fig. 11, we note

the presence of a nonzero time-mean vorticity within the envelope of convergence, consistent with the growing, slow-moving eddies seen in Fig. 13. A point of departure from Fig. 11 is the significant contribution to the vorticity growth from the term  $-(\bar{\zeta} + \beta y)D'$ , particularly away from the equator. In this region, the eddies are able to take advantage of the background vorticity associated with the large cyclonic gyre in the basic state (Fig. 5b). From Fig. 16c, it is evident that the term  $-\zeta'D$  contributes to vorticity growth near the equator, where energy accumulation aids in the wave amplification.

The time-mean kinetic energy and enstrophy for this simulation are presented in Fig. 17. In this case, the off-equatorial parts of the MRG wave exhibit much greater amplification than what is seen at the equator. To further examine the mechanism of the wave growth, we construct the kinetic energy tendency equation from the expressions (8)–(10), which can be written as

$$\begin{aligned} \frac{\partial K'}{\partial t} = & -\bar{\mathbf{u}} \cdot \nabla K' - \mathbf{g}\mathbf{u}' \cdot \nabla h' - u'u' \frac{\partial \bar{u}}{\partial x} - u'v' \frac{\partial \bar{u}}{\partial y} \\ & - u'v' \frac{\partial \bar{v}}{\partial x} - v'v' \frac{\partial \bar{v}}{\partial y}, \end{aligned} \tag{16}$$

where  $K' = (1/2)(u'^2 + v'^2)$  is the eddy kinetic energy. The first two terms on the rhs of (16) are, respectively, the advection of eddy kinetic energy by the background flow and the work done by the eddy geopotential. The last four terms, commonly referred to as the barotropic conversion terms, encapsulate the mechanisms by which energy is exchanged between eddies and the background. The two most dominant barotropic conversion terms as well as the sum of all the terms on the rhs of

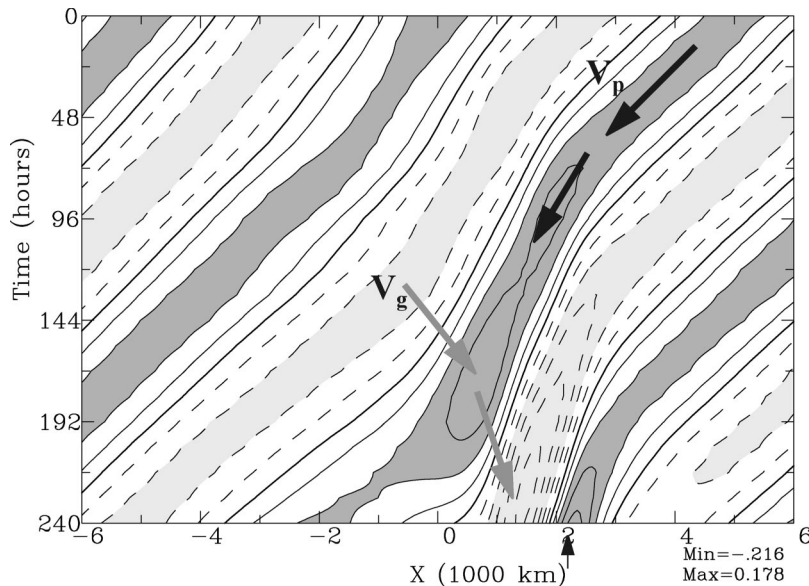


FIG. 15. As in Fig. 10, except for the evolution of the MRG wave in the B2 (asymmetric) basic state.

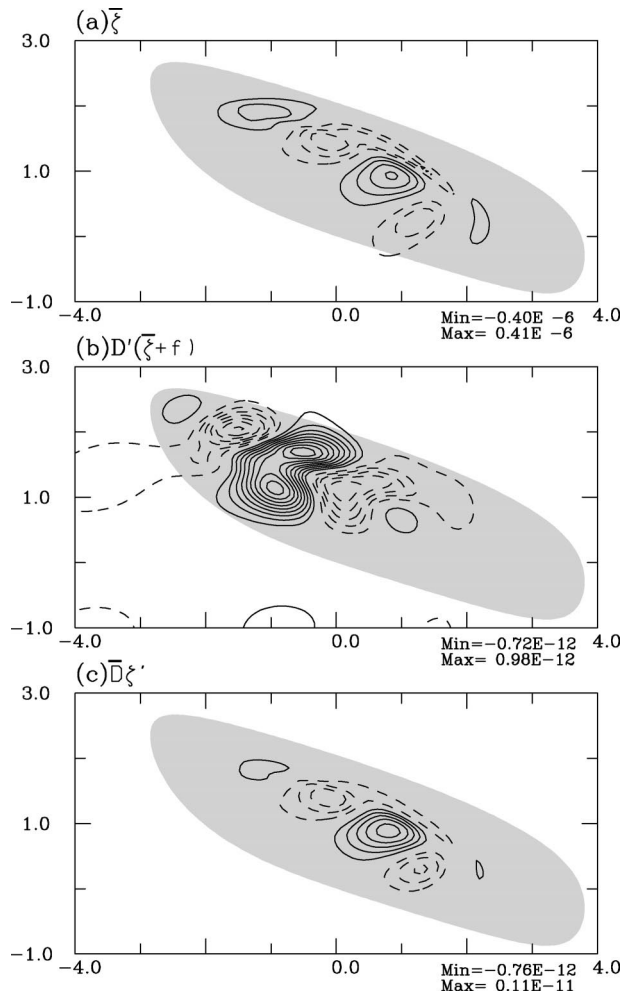


FIG. 16. As in Fig. 11, except for the evolution of the MRG wave in the B2 (asymmetric) basic state. Domain shown is 8000 km  $\times$  4000 km.

(16), averaged over 240 h of the simulation, are shown in Fig. 18. The term  $-u'u'(\partial\bar{u}/\partial x)$  contributes the most particularly near the equator. This term is related to the accumulation of wave energy in a background with zonally reversing flow (e.g., Hartmann and Maloney 2001). The contribution from the term  $-u'v'(\partial\bar{u}/\partial y)$  is also significant. This term is both a sink and a source of energy for the eddies, depending on the interplay between the tilt of the eddies and the basic-state zonal wind shear. As seen in Fig. 18b, this term leads to loss of eddy energy near the equator and generation of the same away from the equator. Figure 18c shows the sum of all the terms that are involved in the eddy kinetic energy tendency. We note that within the region of basic-state convergence, the net effect of all the terms in the kinetic energy tendency equation is to transfer energy from the basic state to the eddies. The small-scale structures in Fig. 18c are reflections of amplifying slow-moving eddies seen in Fig. 13, and these results are

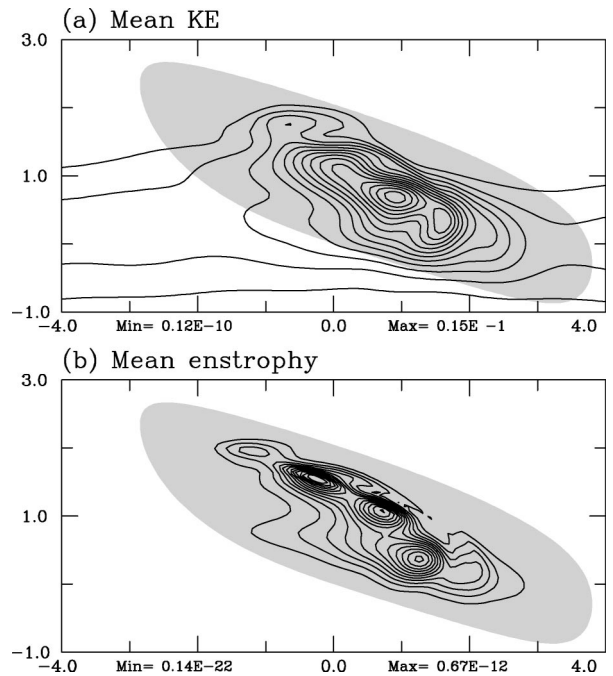


FIG. 17. As in Fig. 12, except for the evolution of the MRG wave in the B2 (asymmetric) basic state. Domain shown is 8000 km  $\times$  4000 km.

consistent with those based on the vorticity budget discussed earlier.

## 6. Sensitivity experiments

The results described in the preceding section have shown that the MRG wave evolution in an asymmetric background differs significantly from the evolution in a symmetric background. The notable features of the development in the asymmetric basic state are the off-equatorial amplification of the MRG wave and the development of small-scale eddies. It is of importance to clarify the extent to which this outcome is dependent on the choice of the scale and structure of the mass sink and the MRG wave. To this end, the following experiments were also performed (see appendix B for details):

- sensitivity to the wavelength of the MRG wave,
- sensitivity to the scale of the mass sink,
- evolution of a localized MRG wave packet, and
- sensitivity to the tilt of the mass sink.

As described in appendix B, changing the scale of the mass sink and the wavelength of the MRG wave creates some differences in the evolution of the MRG wave. In each case, however, off-equatorial disturbances develop that are of the right scale to serve as seedlings for tropical cyclones. Thus, despite the differences, the conclusions drawn from these numerical experiments do not depend on a particular choice of basic state and MRG wave parameters.

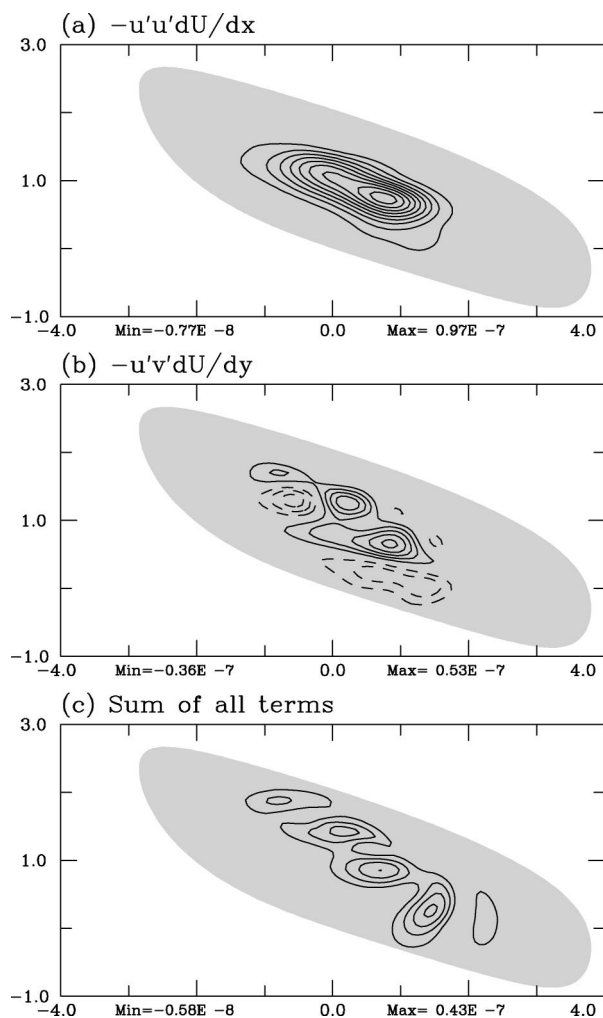


FIG. 18. The barotropic conversion terms averaged over the 240 h of simulation for the evolution of the MRG wave in the B2 (asymmetric) basic state: (a)  $-u'u'dU/dx$ , (b)  $-u'v'dU/dy$ , and (c) sum of all terms. Contour interval in each is  $0.1 \times 10^{-7} \text{ m}^2 \text{ s}^{-1}$ . The shaded area denotes basic-state convergence.

## 7. Discussion

The evolution of MRG waves in idealized MJO environments is examined using a linear shallow water model. The active phase of the MJO is represented by the steady-state response of the tropical atmosphere to localized heating and frictional damping. In the shallow water model, a mass sink is used to simulate the effect of the convective heating associated with the MJO. The initial fields for the MRG waves are obtained analytically following the method outlined by Zehnder (1991). Results for two different mass sink structures are examined in detail.

The method followed in this study is that of an initial value problem. Past studies that have examined similar issues have utilized forcings that were either stochastic or were specified at a boundary (e.g., Kuo et al. 2001; Hartmann and Maloney 2001) and involved long-term

simulations using nondivergent barotropic models. The use of a shallow water model allows us to consider divergent perturbations—specifically MRG waves. Our approach has allowed us to study the evolution of MRG waves through simulations of short duration in a fashion similar to a synoptic examination of the development. However, the current framework does suffer from several limitations. Although, in nature the MJO propagates eastward, the background state in the model is constrained to be invariant in time. An assumption is made that the 10-day simulation period is short enough that the MJO variability is not crucial to the conclusions drawn herein. Furthermore, the use of a single-layered model precludes the inclusion of vertical structures. A more realistic representation of the evolution would also need to consider nonlinear effects and wave-scale convection. However, despite these shortcomings, the simulations provide some insight into the growth of off-equatorial disturbances from MRG waves.

When a symmetric mass sink with maximum amplitude at the equator is used, the resulting steady state and the evolution of the MRG wave are each also symmetric. The MRG wave amplifies within the envelope of convergence in the basic state, and a wave-packet-like structure develops. The zonal scale of the MRG wave decreases in response to the zonally opposing basic-state flow. The reduction in the wavelength is accompanied by amplification of the wave and a slowing of the group speed associated with the wave packet. The maximum amplitude at all stages of the simulation is found at the equator, consistent with the initial structure of the MRG wave. Results from this simulation suggest that a symmetric MJO leads to symmetric growth of the MRG wave and may not be instrumental in the development of localized off-equatorial disturbances.

When an asymmetric mass sink (an idealization of the convective signal associated with an observed MJO event) is used, both the steady-state response and the MRG wave exhibit significant asymmetries. Salient features of this simulation include amplification of the MRG wave and development of a series of smaller-scale, off-equatorial eddies. These off-equatorial disturbances appear as a series of cyclonic and anticyclonic gyres that move toward the northwest at a speed that is slower than the phase speed of the MRG wave. These eddies may represent TD-type disturbances that are commonly observed in the western Pacific (Liebmann and Hendon 1990; Takayabu and Nitta 1993; Dunkerton and Baldwin 1995). These results also bear some resemblance to the development of TD disturbances from MRG waves described by Dickinson and Molinari (2002). However, the off-equatorial disturbances seen in the simulations do not appear to be a result of a complete transformation of the MRG wave. Instead, they appear to be remnants of the amplified parts of the MRG wave that are left behind while the wave continues its motion across the MJO environment. The off-equatorial eddies also seem to retain a memory of their orig-

inal MRG wave structure—a feature also reported by Dickinson and Molinari (2002) in their case study. These results suggest that the symmetry of MRG waves can be broken if the basic states within which they evolve contain persistent asymmetries. Such asymmetrical environments can occur in association with slowly varying large-scale tropical heating that lies predominantly on one side of the equator. Besides the MJO, sources of such quasi-stationary convection may include monsoon troughs.

Additional simulations are also performed to examine the sensitivity of the results to factors such as the wavelength and structure of the MRG wave, and scale and shape of the background convergence. While these factors lead to some differences in the structure of the off-equatorial eddies, the results are qualitatively similar to those described above. In each case, the prominent result is the asymmetric amplification of the MRG wave leading to the development of small-scale eddies off the equator.

The idealized experiments show that, in the presence of an MJO, initially weak MRG waves can amplify and may lead to the development of off-equatorial disturbances from a purely equatorial mode. The scale of these disturbances is considerably smaller than the initial wavelength of the MRG wave and it is possible that the cyclonic elements among them could serve as precursors to tropical cyclones. This process may be particularly relevant to cyclogenesis in the tropical western Pacific, a region that is influenced by the MJO and where MRG waves are frequently observed.

*Acknowledgments.* This work is supported by National Science Foundation Grant ATM 0201752 and Office of Naval Research Grant N00014-02-10821. We wish to thank Dr. Lloyd Shapiro, Dr. Michael Reeder, and Dr. Michael Dickinson for several informative discussions. We are also grateful to two anonymous reviewers for their constructive comments.

## APPENDIX A

### MRG Waves in an Equatorial $\beta$ -Plane Channel

A complete set of solutions of the shallow water equations that describe wave modes in an equatorial  $\beta$  plane was first derived by Matsuno (1966). Following Matsuno (1966), we begin by considering the shallow water equations linearized about a quiescent basic state. By setting the basic-state terms identically to zero in equations (8)–(10), we get

$$\frac{\partial u'}{\partial t} - \beta y v' = -g \frac{\partial h'}{\partial x}, \quad (\text{A1})$$

$$\frac{\partial v'}{\partial t} + \beta y u' = -g \frac{\partial h'}{\partial y}, \quad (\text{A2})$$

$$\frac{\partial h'}{\partial t} + H \left( \frac{\partial u'}{\partial x} + \frac{\partial v'}{\partial y} \right) = 0. \quad (\text{A3})$$

As in Matsuno (1966), we seek plane wave solutions of the form

$$[u', v', h'] = [\tilde{u}(y), \tilde{v}(y), \tilde{h}(y)] e^{i(kx - wt)}, \quad (\text{A4})$$

where  $k$  is the zonal wavenumber and  $w$  is the frequency. Upon substituting these solutions in (A1)–(A3) and rearranging terms, the following equation for  $\tilde{v}$  is obtained:

$$\frac{\partial^2 \tilde{v}}{\partial y^2} + \left( \frac{w^2}{c^2} - \frac{k\beta}{w} - k^2 - \frac{\beta^2 y^2}{c^2} \right) \tilde{v} = 0, \quad (\text{A5})$$

where  $c = (gH)^{1/2}$  is the pure gravity wave speed. To investigate wave motions near the equator, Matsuno (1966) stipulated that the meridional velocity components vanish far away from the equator; that is,

$$v \rightarrow 0; \quad y \rightarrow \pm \infty. \quad (\text{A6})$$

Provided  $k$  and  $w$  satisfy the condition

$$\frac{w^2}{c^2} - \frac{k\beta}{w} - k^2 - \frac{\beta^2 y^2}{c^2} = 2n + 1 \quad n = 0, 1, 2, \dots, \quad (\text{A7})$$

the solution of (A5) is given by

$$\tilde{v}(y) = A e^{(-1/2y^2)} H_n(y), \quad (\text{A8})$$

where  $H_n(y)$  is the  $n$ th-order Hermitian polynomial. However, in the shallow water model, we require that the wave solutions be confined to a channel of finite width. Thus, the meridional velocity, now constrained to vanish at the northern and southern boundaries of the domain, yields the condition

$$v \rightarrow 0; \quad y \rightarrow \pm D. \quad (\text{A9})$$

A solution of (A5), subject to the boundary condition (A9) was obtained by Koss (1967) and modified for a single homogeneous layer of fluid by Zehnder (1991). Following Zehnder (1991), but retaining the dimensional forms of the variables, the expressions for the velocity components and the free surface height for the MRG mode can be derived to be

$$v'(x, y, t) = A \phi_1 e^{-\beta y^2/2c} \cos(kx - wt), \quad (\text{A10})$$

$$u'(x, y, t) = A \beta y \frac{e^{-\beta y^2/2c}}{(k^2 c^2 - w^2)} [(w + ck)\phi_1 + 2ck\alpha\phi_1^*] \times \sin(kx - wt), \quad \text{and} \quad (\text{A11})$$

$$h'(x, y, t) = A \beta y c \frac{e^{-\beta y^2/2c}}{g(k^2 c^2 - w^2)} \times [(w + ck)\phi_1 + 2w\alpha\phi_1^*] \sin(kx - wt), \quad (\text{A12})$$

where  $A$  is an arbitrary amplitude factor, while  $\phi_1$  and  $\phi_1^*$  denote confluent hypergeometric functions such that

$$\phi_1 = \phi\left(-\frac{\alpha}{2}, \frac{1}{2}; \frac{\beta y^2}{c}\right) \quad \text{and} \quad (\text{A13})$$

$$\phi_1^* = \phi\left(1 - \frac{\alpha}{2}, \frac{3}{2}; \frac{\beta y^2}{c}\right), \quad (\text{A14})$$

with  $\alpha$  defined as

$$\alpha = \frac{w^3 - c^2 k \beta - c^2 w k^2 - \beta w c}{2\beta c w}. \quad (\text{A15})$$

Equation (A15) is the dispersion relation for the equatorial MRG mode confined in a channel. The initial ( $t = 0$ ) fields for the MRG wave mode are obtained as follows.

- For the channel domain, the condition  $v \rightarrow 0$ ;  $y \rightarrow \pm D$  is invoked to set  $v'(x, D, 0) = 0$ , where  $D = 4000$  km. Consequently, from (A10) and (A13), we require

$$\phi\left(-\frac{\alpha}{2}, \frac{1}{2}; \frac{\beta D^2}{c}\right) = 0. \quad (\text{A16})$$

The root  $\alpha$  that satisfies (A16) is obtained numerically.<sup>A1</sup>

- Once  $\alpha$  is determined and a suitable wavenumber ( $k$ ), is chosen, (A15) is solved to obtain the frequency ( $w$ ) of the MRG wave.<sup>A2</sup>
- At this point, all the required parameters in (A10)–(A12) are known and the initial fields for the MRG wave in a quiescent environment are computed.

## APPENDIX B

### Sensitivity Experiments

In this section we briefly examine the sensitivity of the results discussed in the paper to factors such as the wavelength and structure of the MRG perturbations as well as the scale of the MJO. To avoid confusion with with figure references, the B2 basic state (Fig. 5) will be referred to as the asymmetric basic state.

#### a. Sensitivity to the wavelength of the MRG wave

Figure B1 shows the close-up view of the height field associated with the eddies that result after 240 h within the asymmetric basic state for MRG waves of wavelength 8000 km (Fig. B1a) and 10 000 km (Fig. B1b). A comparison with Fig. 14 shows that the resulting structures are qualitatively similar although the strength of the eddies differs for the three different wavelengths:

<sup>A1</sup> Multiple roots of (A16) exist. Choosing the first root yields wave structures with the largest possible meridional extent within the channel:  $-D \leq y \leq D$  (Zehnder 1991).

<sup>A2</sup> Equation (A15), being cubic, yields three roots and only one of them corresponds to the westward-moving MRG wave.

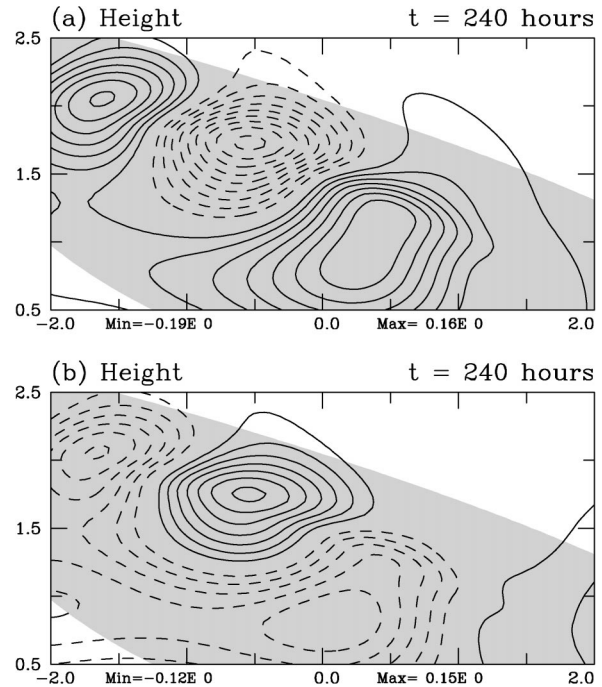


FIG. B1. Sensitivity to the wavelength of the MRG wave: close-up view of the height field (contour interval 0.02 m) of MRG wave of wavelength (a) 8000 km and (b) 10 000 km after 240 h of evolution within the B2 (asymmetric) basic state. Domain shown is  $4000 \text{ km} \times 3000 \text{ km}$ .

strongest for 5000-km wave and weakest for the 10 000-km wave. Both the 8000-km wave and the 10 000-km wave have a faster westward phase speed and consequently shorter residence time within the background convergence, which affects the extent of the amplification of the wave. Kuo et al. (2001) also found that larger wavelengths lead to insufficient scale contraction and reduced energy accumulation of Rossby waves within a convergent background.

Despite the quantitative differences seen in Fig. 14 and Fig. B1, the results suggest that, for the range of MRG wavelengths that are commonly observed in the central and western Pacific, the outcome of the evolution in the idealized MJO background is qualitatively similar in each case: the generation of off-equatorial small-scale disturbances that could represent seedlings of tropical cyclones.

#### b. Sensitivity to the scale of the basic-state convergence

Results from the variation of the meridional scale of the mass sink on the development of the wavenumber 8 MRG wave are shown in Fig. B2. In both cases the mass sink used (Fig. 4) to obtain the asymmetric basic state is modified. When the meridional scale of the mass sink is reduced by 50%, off-equatorial development of the MRG wave still occurs, although the resulting eddies

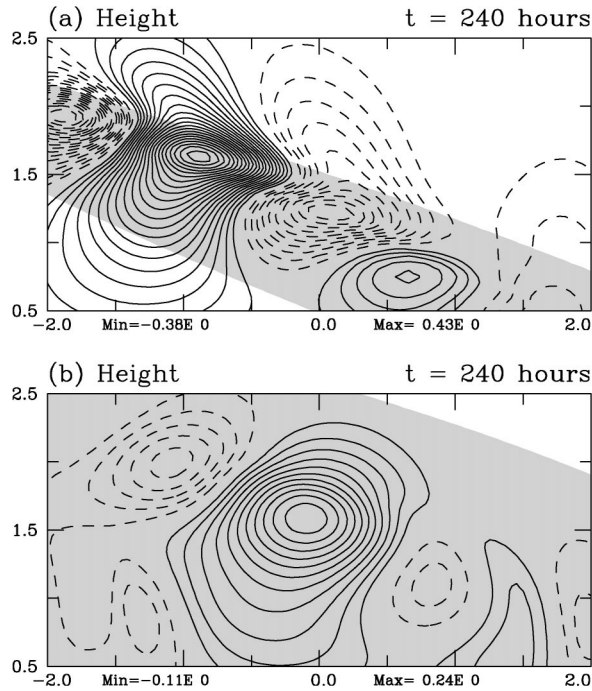


FIG. B2. Sensitivity to the meridional scale of the background convergence: close-up view of the height field (contour interval 0.02 m) of the wavenumber-8 MRG wave after 240 h of evolution in (a) thinner and (b) wider versions of the B2 (asymmetric) basic state. Domain shown is 4000 km  $\times$  3000 km.

are considerably deformed (Fig. B2a). The eddies are stronger in amplitude compared to those in Fig. 14b since a more compact mass sink leads to stronger background convergence. If instead the mass sink is made 50% wider, the background convergence has a larger meridional extent and the eddies are somewhat more axisymmetric (Fig. B2b). Extending the zonal scale of the mass sink yields almost identical results to the ones shown in Fig. 14 (not shown).

The results shown in Fig. B2 suggest that the scale of the background convergence has some effect on the structure of the eddies, although once again, off-equatorial development on a scale smaller than the initial wave is seen in each case.

#### c. Evolution of an MRG wave packet in asymmetric basic state

We also perform a simulation wherein, instead of a global pure wave mode, we prescribe a localized MRG wave packet at the initial time. The objective of this exercise is to examine the evolution of a wave packet that is initially located away from the bulk of the basic-state forcing, and its development as it moves within the active MJO. The initial wave packet structure is created by modulating the MRG wave solution shown in Fig. 1 by a cosine function.

In a quiescent basic state, the wave packet propagates

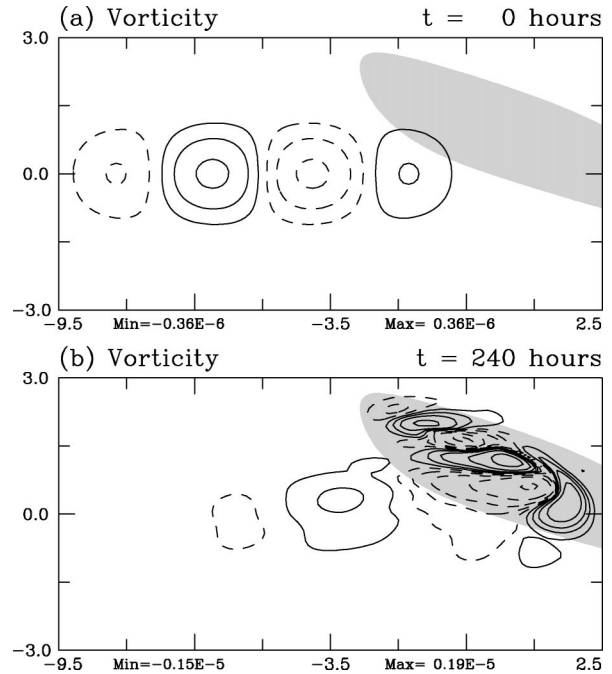


FIG. B3. Vorticity at (a)  $t = 0$  h and (b)  $t = 240$  h of an MRG wave packet in the asymmetric basic state. Domain shown is 12 000 km  $\times$  6000 km. Contour interval is as in Fig. 9.

to the east at its group speed while individual crests and troughs move westward within its envelope (not shown). In the presence of the MJO background, the evolution of the wave packet is significantly different. For the sake of brevity only the vorticity fields at 0 and 240 h from this simulation are shown (Fig. B3). When Fig. B3 is compared with Fig. 13, it is evident that the development of the disturbances within the wave packet is qualitatively similar to that for the wave. As in the previous case, a series of small-scale northwest-to-southeast-oriented eddies has developed. The eastward propagation of the wave packet has been impeded while the scale of the packet has decreased after 240 h of simulation. Similarities in the two cases are also noted when the Hovmöller diagrams and the energy budgets are compared (not shown).

#### d. Sensitivity to the tilt of the mass sink

The preceding discussions have highlighted the role of an asymmetric environment in both the amplification of the MRG wave as well as the development of off-equatorial eddies. While the choice of the tilted mass sink structure that produced the asymmetric basic state was based on an idealization of an observed MJO event, we also considered mass sinks of other orientations.

As a brief illustration, results are presented from a simulation with a basic state that was driven by heating that is confined within one hemisphere (Fig. B4). The mass sink that produced this basic state is identical to the one shown in Fig. 2, except that it is translated

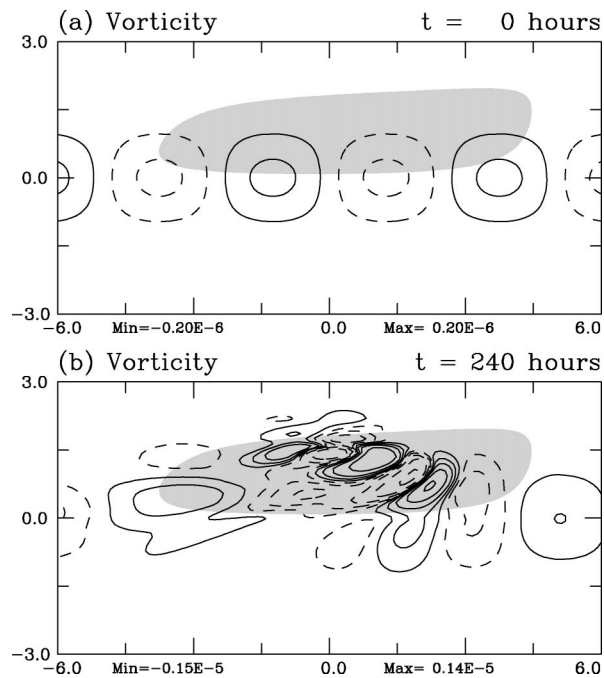


FIG. B4. As in Fig. 13, except for the evolution of the MRG wave in a basic state obtained from a mass sink that lies entirely in the Northern Hemisphere after (a) 0 h and (b) 240 h. Domain shown is 12 000 km  $\times$  6000 km.

meridionally to lie entirely within the Northern Hemisphere. As evident from Fig. B4, several features seen in Fig. 13 are present in this case, prominent among them being the development of off-equatorial eddies. The eddies in Fig. B4 also show evidence of a northwest-southeast alignment, although, when compared with Fig. 13d, we note that their tilt is less prominent—a result of the basic-state gyre being more elongated along the horizontal (not shown).

This result shows that the background heating need not have a specific tilt with respect to the equator in order to produce off-equatorial eddies. While the details of the alignment of the eddies may depend on the tilt, it is the asymmetry of the heating that is most influential in the off-equatorial development of the MRG wave.

#### REFERENCES

- Chang, C.-P., J. M. Chen, P. A. Harr, and L. E. Carr, 1996: Northwestward propagating wave patterns over the tropical western North Pacific during summer. *Mon. Wea. Rev.*, **124**, 2245–2266.
- Dickinson, M., and J. Molinari, 2002: Mixed Rossby-gravity waves and western Pacific tropical cyclogenesis. Part I: Synoptic evolution. *J. Atmos. Sci.*, **59**, 2183–2196.
- Dunkerton, T. J., and M. P. Baldwin, 1995: Observation of 3–6-day meridional wind oscillations over the tropical Pacific, 1973–1992: Horizontal structure and propagation. *J. Atmos. Sci.*, **52**, 1585–1601.
- Farrell, B., and I. Watterson, 1985: Rossby waves in opposing currents. *J. Atmos. Sci.*, **42**, 1746–1756.
- Ferreira, R. N., W. H. Schubert, and J. J. Hack, 1996: Dynamical aspects of twin tropical cyclones associated with the Madden-Julian oscillation. *J. Atmos. Sci.*, **53**, 929–945.
- Gill, A. E., 1980: Some simple solutions for heat-induced tropical circulation. *Quart. J. Roy. Meteor. Soc.*, **106**, 447–462.
- Hartmann, D. L., and E. D. Maloney, 2001: The Madden-Julian oscillation, barotropic dynamics, and North Pacific tropical cyclone formation. Part II: Stochastic barotropic modeling. *J. Atmos. Sci.*, **58**, 2559–2570.
- Heckley, W. A., and A. E. Gill, 1984: Some simple analytical solutions to the problem of forced equatorial long waves. *Quart. J. Roy. Meteor. Soc.*, **110**, 203–217.
- Koss, W. J., 1967: Further theoretical considerations of tropospheric wave motions in equatorial latitudes. *Mon. Wea. Rev.*, **95**, 283–297.
- Kuo, H.-C., J.-H. Chen, R. T. Williams, and C.-P. Chang, 2001: Rossby waves in zonally opposing mean flow: Behavior in the Northwest Pacific summer monsoon. *J. Atmos. Sci.*, **58**, 1035–1050.
- Lau, K.-H., and N.-C. Lau, 1990: Observed structure and propagation characteristics of tropical summertime disturbances. *Mon. Wea. Rev.*, **118**, 1888–1913.
- Liebmann, B., and H. H. Hendon, 1990: Synoptic-scale disturbances near the equator. *J. Atmos. Sci.*, **47**, 1463–1479.
- Madden, R. A., and P. R. Julian, 1994: Observations of the 40–50-day oscillation—A review. *Mon. Wea. Rev.*, **122**, 814–837.
- Maloney, E. D., and D. L. Hartmann, 2001: The Madden-Julian oscillation, barotropic dynamics, and North Pacific tropical cyclone formation. Part I: Observations. *J. Atmos. Sci.*, **58**, 2845–2558.
- Matsuno, T., 1966: Quasi-geostrophic motions in the equatorial area. *J. Meteor. Soc. Japan*, **44**, 25–43.
- Nakazawa, T., 1986: Tropical super clusters within intraseasonal variations over the western Pacific. *J. Meteor. Soc. Japan*, **64**, 17–33.
- Shapiro, L. J., 1977: Tropical storm formation from easterly waves: A criterion for development. *J. Atmos. Sci.*, **34**, 1007–1021.
- , 1980: The effect of nonlinearities on the evolution of barotropic easterly waves in a nonuniform environment. *J. Atmos. Sci.*, **37**, 2631–2643.
- Straub, K. H., and G. N. Kiladis, 2003: Interaction between the boreal summer intraseasonal oscillation and higher-frequency tropical wave activity. *Mon. Wea. Rev.*, **131**, 945–960.
- Sobel, A. H., and C. S. Bretherton, 1999: Development of synoptic-scale disturbances over the summertime tropical northwest Pacific. *J. Atmos. Sci.*, **56**, 3106–3127.
- , and E. D. Maloney, 2000: Effect of ENSO and the MJO on western North Pacific tropical cyclones. *Geophys. Res. Lett.*, **27**, 1739–1742.
- Sui, C.-H., and K.-M. Lau, 1992: Multiscale phenomena in the tropical atmosphere over the western Pacific. *Mon. Wea. Rev.*, **120**, 407–430.
- Takayabu, Y. N., and T. Nitta, 1993: 3–5 day disturbances coupled with convection in over the Tropical Pacific Ocean. *J. Meteor. Soc. Japan*, **71**, 221–245.
- Wallace, J. M., and V. E. Kousky, 1968: Observational evidence of Kelvin waves in the tropical atmosphere. *J. Atmos. Sci.*, **25**, 900–907.
- Webster, P. J., 1972: Response of the tropical atmosphere to local, steady forcing. *Mon. Wea. Rev.*, **100**, 518–541.
- , and H.-R. Chang, 1988: Equatorial energy accumulation and emanation regions: Impacts of a zonally varying basic state. *J. Atmos. Sci.*, **45**, 803–829.
- Wheeler, M., and G. N. Kiladis, 1999: Convectively couple equatorial waves: Analysis of clouds and temperature in the wavenumber-frequency domain. *J. Atmos. Sci.*, **56**, 374–399.
- , —, and P. J. Webster, 2000: Large-scale dynamical fields associated with equatorial waves. *J. Atmos. Sci.*, **57**, 613–640.
- Yamagata, T., and Y. Hayashi, 1984: A simple diagnostic model of the 30–50 day oscillation in the Tropics. *J. Meteor. Soc. Japan*, **62**, 709–717.
- Yamazaki, N., and M. Murakami, 1989: An intraseasonal amplitude

- modulation of the short-term tropical disturbances over the western Pacific. *J. Meteor. Soc. Japan*, **67**, 981–807.
- Yanai, M., and T. Maruyama, 1966: Stratospheric wave disturbances propagating over the equatorial Pacific. *J. Meteor. Soc. Japan*, **44**, 291–294.
- Zehnder, J. A., 1991: The interaction of planetary-scale tropical easterly waves with topography: A mechanism for the initiation of tropical cyclones. *J. Atmos. Sci.*, **48**, 1217–1230.
- Zhang, Z., and T. N. Krishnamurti, 1996: A generalization of Gill's heat-induced tropical circulation. *J. Atmos. Sci.*, **53**, 1045–1052.